AGU PUBLICATIONS

JGR

Journal of Geophysical Research: Atmospheres

RESEARCH ARTICLE

10.1002/2014JD021641

Key Points:

- Sources and evolution processes of a record-breaking haze episode
- Large increase of coal combustion organic aerosol during haze episodes
- Estimation of regional contributions from steep increases of aerosol species

Supporting Information:

- Figures S1–S15

Correspondence to:
Y. Sun,
sunyele@mail.iap.ac.cn

Citation:
Sun, Y., Q. Jiang, Z. Wang, P. Fu, J. Li, T. Yang, and Y. Yin (2014), Investigation of the sources and evolution processes of severe haze pollution in Beijing in January 2013, *J. Geophys. Res. Atmos.*, *119*, doi:10.1002/2014JD021641.

Received 13 FEB 2014
Accepted 20 MAR 2014
Accepted article online 25 MAR 2014

Investigation of the sources and evolution processes of severe haze pollution in Beijing in January 2013

Yele Sun[1,2], Qi Jiang[1,3], Zifa Wang[1], Pingqing Fu[1], Jie Li[1], Ting Yang[1], and Yan Yin[2,3]

[1]State Key Laboratory of Atmospheric Boundary Layer Physics and Atmospheric Chemistry, Institute of Atmospheric Physics, Chinese Academy of Sciences, Beijing, China, [2]Collaborative Innovation Center on Forecast and Evaluation of Meteorological Disasters, Nanjing University of Information Science and Technology, Nanjing, China, [3]Key Laboratory for Aerosol-Cloud-Precipitation of China Meteorological Administration, Nanjing University of Information Science and Technology, Nanjing, China

Abstract China experienced severe haze pollution in January 2013. Here we have a detailed characterization of the sources and evolution mechanisms of this haze pollution with a focus on four haze episodes that occurred during 10–14 January in Beijing. The main source of data analyzed is from submicron aerosol measurements by an Aerodyne Aerosol Chemical Speciation Monitor. The average PM1 mass concentration during the four haze episodes ranged from 144 to 300 $\mu g\ m^{-3}$, which was more than 10 times higher than that observed during clean periods. All submicron aerosol species showed substantial increases during haze episodes with sulfate being the largest. Secondary inorganic species played enhanced roles in the haze formation as suggested by their elevated contributions during haze episodes. Positive matrix factorization analysis resolved six organic aerosol (OA) factors including three primary OA (POA) factors from traffic, cooking, and coal combustion emissions, respectively, and three secondary OA (SOA) factors. Overall, SOA contributed 41–59% of OA with the rest being POA. Coal combustion OA (CCOA) was the largest primary source, on average accounting for 20–32% of OA, and showed the most significant enhancement during haze episodes. A regional SOA (RSOA) was resolved for the first time which showed a pronounced peak only during the record-breaking haze episode (Ep3) on 12–13 January. The regional contributions estimated based on the steep evolution of air pollutants were found to play dominant roles for the formation of Ep3, on average accounting for 66% of PM1 during the peak of Ep3 with sulfate, CCOA, and RSOA being the largest fractions ($> \sim 75\%$). Our results suggest that stagnant meteorological conditions, coal combustion, secondary production, and regional transport are four main factors driving the formation and evolution of haze pollution in Beijing during wintertime.

1. Introduction

Haze pollution has become a national interest of the public, government, and atmospheric scientists in China since January 2013. Haze is an atmospheric phenomenon where smoke, dust, moisture, and vapor suspended in air impair visibility [*Watson*, 2002]. Haze not only reduces visibility and affects transportation but also exerts detrimental effects on human health. For example, the number of patients with respiratory and cardiovascular disease increases significantly during the haze episodes [*Zhang et al.*, 2013b]. In January 2013, central eastern China experienced several severe haze episodes with thick smog clouds spreading over millions of square kilometers and affecting the health of millions. In particular, a record-breaking haze episode over the past 60 years occurred in North China Plain (NCP) on 12–13 January. The air pollution was dangerously high with the peak concentration of fine particles ($PM_{2.5}$) exceeding more than 10 times the China National Ambient Air Quality Standard (NAAQS, 75 $\mu g\ m^{-3}$ for 24 h average) that was released in February 2012 by the Ministry of Environmental Protection of China. Therefore, understanding the sources, formation mechanisms, and evolution processes of haze pollution is of importance for making air pollution control measures and assessing its health and climate impacts.

Owing to the growing concern of haze pollution, extensive studies have been conducted in recent years to investigate the sources and formation mechanisms of haze in China [*Sun et al.*, 2006; *An et al.*, 2007; *Li et al.*, 2010; *Ma et al.*, 2010; *Huang et al.*, 2012; *Tao et al.*, 2012; *Liu et al.*, 2013; *Wang et al.*, 2013b; *Zhao et al.*, 2013]. The haze pollution exhibits different characteristics among different seasons. While agricultural burning and photochemical production are two dominant factors influencing the formation of haze in summer

[*Li et al.*, 2010; *Huang et al.*, 2012; *Sun et al.*, 2012], coal combustion is a large source of haze particles during wintertime [*Sun et al.*, 2013b]. Severe haze pollution occurs frequently in winter, due to not only substantial increases of coal combustion emissions for heating but also the frequent occurrence of fog episodes [*Quan et al.*, 2011]. *Sun et al.* [2006] investigated the chemical characteristics of two severe haze-fog episodes in the winter of 2004 in Beijing. The 6 h average $PM_{2.5}$ mass concentration exceeded 300 $\mu g\ m^{-3}$ with secondary inorganic species being the major fraction. The large increases of secondary inorganic species, e.g., sulfate (SO_4^{2-}), nitrate (NO_3^-), and ammonium (NH_4^+), during the haze episodes were also observed at four sites in NCP in January 2010 [*Zhao et al.*, 2013]. Further, all four sites showed synchronous increases of secondary species illustrating a regional characteristic of haze pollution. The formation of severe haze pollution is also strongly dependent on synoptic conditions. The common characteristics of stagnant meteorological parameters, e.g., low wind speed, high humidity, and shallow boundary layer, during severe haze pollution periods have been observed many times at various locations in previous studies [*Sun et al.*, 2006; *Zhao et al.*, 2013]. These results suggest that both meteorological conditions and aerosol chemistry play important roles in haze formation and evolution.

Despite previous efforts in the characterization of haze pollution, our knowledge of its sources and evolution processes is not fully clear yet. The haze pollution often evolves rapidly and dynamically in the atmosphere by involving complex processes such as direct emissions, secondary formation, aging and mixing, and fog processing. The chemical, physical, and optical properties of aerosol particles may change significantly in a few hours. However, previous studies based on filter measurements are limited by either low time resolution from hours to days or sampling artifacts such as evaporative loss. The Aerodyne Aerosol Mass Spectrometer (AMS) is unique in providing size-resolved nonrefractory submicron aerosol (NR-PM_1) species (organics, sulfate, nitrate, ammonium, and chloride) in real time with a high time resolution ranging from seconds to minutes [*Jayne et al.*, 2000; *Canagaratna et al.*, 2007]. As a result, AMSs have been widely used in both field measurements and lab studies since 2000. However, the deployments of the AMS in China started only in recent years [*Huang et al.*, 2010; *Sun et al.*, 2010, 2012]. *Sun et al.* [2010] first characterized the sources, composition, and variations of NR-PM_1 species in Beijing during summer 2006 with a Quadrupole AMS (Q-AMS). *Huang et al.* [2010] and *Sun et al.* [2012] further investigated Beijing submicron aerosols in the summer of 2008 and 2011 with a High-Resolution Time-of-Flight AMS (HR-AMS) and an Aerosol Chemical Speciation Monitor (ACSM), respectively. All NR-PM_1 species varied dramatically during all studies, but overall organic aerosol (OA) constituted the largest fraction of NR-PM_1, contributing on average ~35–40% in summer [*Huang et al.*, 2010; *Sun et al.*, 2010, 2012]. The composition and sources of OA were further investigated with positive matrix factorization (PMF) [*Paatero and Tapper*, 1994]. Various OA components, e.g., hydrocarbon-like OA (HOA), cooking OA (COA), semivolatile oxygenated OA (SV-OOA), and low volatility OOA (LV-OOA) were distinguished. Most previous AMS studies in China were conducted in summer, while these are rare in winter [*Sun et al.*, 2013b]. Because of different meteorological conditions and source emissions, the aerosol particle composition, OA composition, and aerosol processing could be significantly different between summer and winter. Considering that winter is a season with frequent occurrences of haze pollution, a comprehensive understanding of chemical composition, sources, and formation mechanisms of winter haze is essential.

China experienced several severe haze episodes in January 2013. Although a few studies have investigated the severe haze pollution from the perspectives of meteorology [*Wang et al.*, 2013a], chemistry [*Wang et al.*, 2014a], and modeling [*Wang et al.*, 2013b], the sources and evolution processes of the record-breaking haze episode on 12–13 January are not well known. In this study, we present a comprehensive characterization of aerosol particles during the first half-month of January at an urban site in Beijing with a focus on four severe haze episodes during 10–14 January 2013. The chemical evolution of submicron aerosol composition, OA composition, and its relationship with meteorological parameters are investigated in detail. The sources of haze pollution, e.g., primary emissions versus secondary production and local sources versus regional transport, are elucidated. In particular, the regional contributions to the record-breaking haze episode are estimated based on the steep evolution of aerosol species.

2. Experimental

2.1. Sampling Site

All the measurements in this study were conducted at the same site as reported in *Sun et al.* [2013b], i.e., an urban site located at the Institute of Atmospheric Physics (IAP), Chinese Academy of Sciences, between the north third and fourth ring road during 1–16 January 2013. All the gas and aerosol instruments were placed in a room on the top of a two-story building (~ 8 m high). The sampling site is approximately 380 m from the nearest Jingzang highway. Meteorological parameters at 15 different heights (from 8 m to 320 m), including wind speed, wind direction, relative humidity (RH), and temperature, were obtained from a 325 m meteorological tower located nearby. In addition, other meteorological parameters, e.g., solar radiation and pressure, were obtained from a ground meteorological station at IAP. More detailed descriptions of the sampling site can be found in *Sun et al*. [2012, 2013b].

2.2. Instrumentation

The ambient air was drawn inside the sampling room through a stainless steel tube (outer diameter: 0.0127 m) at a flow rate of 3 L/min, of which ~0.1 L/min was subsampled to an ACSM and 0.85 L/min to a Cavity Attenuated Phase Shift extinction monitor (CAPS PM_{ext}, Aerodyne Research Inc.). A $PM_{2.5}$ URG cyclone (URG-2000-30ED) was employed in front of the sampling line to remove coarse particles, and a silica gel dryer was used to dry aerosol particles that enter the ACSM and the CAPS. The NR-PM_1 species including organics, sulfate, nitrate, ammonium, and chloride were measured in situ by the ACSM at a time resolution of ~15 min. The detailed operations and calibrations of the ACSM have been given in detail in *Sun et al*. [2013b]. Because of the limited vaporizer temperature (~600 °C), the ACSM cannot measure refractory black carbon (BC) component. Thus, a 2-wavelength Aethalometer (Model AE22, Magee Scientific Corporation) was employed to measure the BC in $PM_{2.5}$ at a time resolution of 5 min.

The CAPS PM_{ext} was deployed to measure the light extinction (630 nm) of dry aerosol particles at a time resolution of 1 s. The CAPS PM_{ext} measures the phase shift (ϑ) of a distorted waveform of the modulated light from a light emitting diode (LED) in the sample cell with two high reflectivity mirrors. The relationship between ϑ and light extinction (σ_{ext}) is described as

$$\cot\vartheta = \cot\vartheta_0 + \frac{c}{2\pi f}\sigma_{ext} \quad (1)$$

where c is the speed of light, f is the LED modulation frequency, and ϑ_0 is the sensor response of particle-free air. The detailed principles of the CAPS technology can be found in *Kebabian et al*. [2008].

A suite of commercial gas analyzers from Thermo Scientific was used to measure the gaseous species including carbon monoxide (CO), ozone (O_3), nitrogen monoxide (NO), total reactive nitrogen (NO_y), and sulfur dioxide (SO_2), and a Tapered Element Oscillating Microbalance (TEOM series1400a, Thermo Scientific) was used to determine the $PM_{2.5}$ mass concentration. All the data were reported at 1 min time resolution. Moreover, a CAPS NO_2 monitor utilizing the same technology as the CAPS PM_{ext} was used to measure the ambient nitrogen dioxide (NO_2) at a time resolution of 1 s [*Ge et al*., 2013]. In addition, a dual-wavelength (532 and 1064 nm) depolarization lidar (Model: L2S-SM II, NIES Japan) was deployed to measure backscattering coefficients and depolarization ratio with a time interval of 15 min and a vertical resolution of 30 m. The detailed lidar operations and data analysis were given in *Yang et al*. [2010].

All the data in this study are reported as Beijing local time which equals the Coordinated Universal Time (UTC) plus 8 h.

2.3. ACSM Data Analysis

The mass concentration and chemical composition of NR-PM_1 species were analyzed with the ACSM standard data analysis software (v 1.5.3.0, https://sites.google.com/site/ariacsm/mytemplate-sw) within Igor Pro (WaveMetrics, Inc., Oregon, USA). Similar to previous ACSM data analysis in Beijing [*Sun et al*., 2012, 2013b], a collection efficiency (CE) of 0.5 was applied to account for the incomplete detection of particles primarily due to particle bounce [*Matthew et al*., 2008], and a relative ionization efficiency (RIE) of 6.5 was used for ammonium quantification. The average ratio of PM_1 (NR-PM_1 + BC) / $PM_{2.5}$ (0.71, Figure S1) in this study is overall consistent with the values observed in our previous studies [*Sun et al*., 2012, 2013b] suggesting that the CE of 0.5 is appropriate. In addition, a relative ion transmission efficiency (RIT) was introduced to correct the data between m/z 50 and 150 [*Ng et al*., 2011b]. While a linear relationship between RIT and m/z was appropriate for our early ACSM data analysis, the exponential relationship showing the best fit after one year's deployment was used in this study.

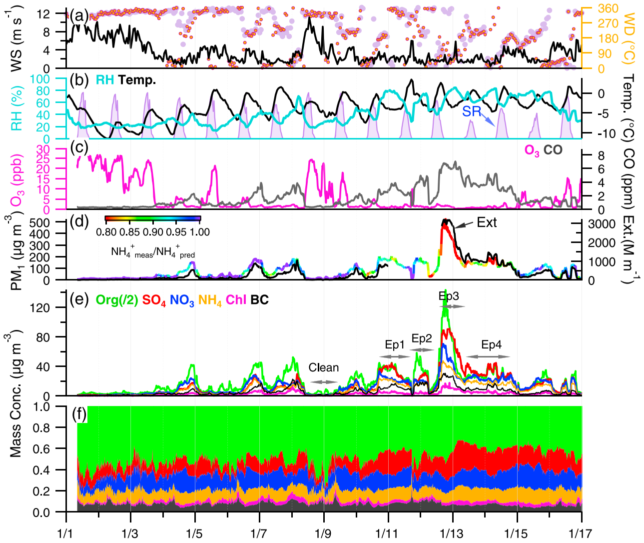

Figure 1. Time series of (a) wind speed (WS) and wind direction (WD) at the height of 120 m, (b) relative humidity (RH), temperature (Temp), and solar radiation (SR), (c) gaseous O_3 and CO, (d) PM_1 (= NR-PM_1 + BC) and extinction coefficient of $PM_{2.5}$, (e) aerosol species in PM_1, and (f) mass fraction of each species in PM_1. The WD at 320 m is also shown in Figure 1a as blue solid circles. The time series of PM_1 in Figure 1d is color coded by aerosol particle acidity indicated as $NH_{4\,meas}^{+}/NH_{4\,pred}^{+}$. In addition, one clean period and four haze episodes are marked in Figure 1e for further discussions.

The ACSM organic mass spectra were analyzed by positive matrix factorization (PMF) to resolve potential OA components with different sources and processes. The PMF analysis with the algorithm PMF2.exe [*Paatero and Tapper*, 1994] was performed on the OA mass spectra matrix between *m/z* 12 and 120. The *m/z*'s above 120 with interferences from naphthalene signals and larger uncertainties due to the RIT corrections were excluded from the PMF analysis. The PMF results were then evaluated using the PMF Evaluation Tool (PET, v 2.06) [*Ulbrich et al.*, 2009] following the procedures detailed in *Zhang et al.* [2011a]. More detailed PMF diagnostics are presented in Figures S2–S7. After a careful evaluation of the mass spectral profiles, diurnal variations, and time series of OA components, and also comparisons to OA factors resolved during wintertime 2011–2012 [*Sun et al.*, 2013b], a six-factor solution with fpeak = −0.8 was selected. The six OA factors include three primary factors, i.e., hydrocarbon-like OA (HOA), cooking OA (COA), and coal combustion OA (CCOA), and three secondary factors, i.e., semivolatile OOA (SV-OOA), local secondary OA (LSOA), and regional SOA (RSOA).

3. Results and Discussion

3.1. General Descriptions of the Haze Episodes in January

Figure 1 shows the time series of meteorological parameters and submicron aerosol composition during 1–16 January 2013. The aerosol composition varied dramatically and was strongly associated with meteorological conditions throughout the entire study, during which four periods with different aerosol evolution processes were observed. The first period of 1–3 January shows typical characteristics of clean days with low PM_1 mass loading (generally $< 20\ \mu g\ m^{-3}$) and dominant organic contribution (~60%) [*Sun et al.*, 2013b]. This clean period was characterized by the prevailing northerly winds, high wind speed ($> 4\ m\ s^{-1}$), and low relative humidity (~20–30%), which are all favorable conditions for the dispersion of air pollutants. The second period of 4–8 January was characterized by three evident pollution episodes, each of which lasted less than 1 day. The evolution of the three episodes was similar with the formation starting from a wind direction change from northerly to southerly at ~ 9:00. The PM_1 during the three episodes evolved rapidly and reached its maximum (~150–190 $\mu g\ m^{-3}$) in half a day and was then cleared out by a return to northerly winds.

After a short period of another clean episode (12:00, 8 January to 6:00, 9 January), a long and heavily PM-polluted episode dominated the rest of the study. The wind speed was generally low ($< 2\ m\ s^{-1}$), yet the relative humidity was higher than the previous three pollution episodes with most of the time being in the range of ~60–80% (Figure 1). The MODIS satellite images also showed thick clouds over the North China Plain during this period, and correspondingly, foggy days were reported almost every day (http://www.weather.com.cn/weather/101010100.shtml). Likely due to the persistently stagnant meteorological conditions, the PM_1 concentration remained consistently high ($> 150\ \mu g\ m^{-3}$) and hit a record of $> 500\ \mu g\ m^{-3}$ at ~18:00 on 12 January [*Huang et al.*, 2010; *Sun et al.*, 2010; *Zhang et al.*, 2011b; *Sun et al.*, 2012, 2013b] when the visibility

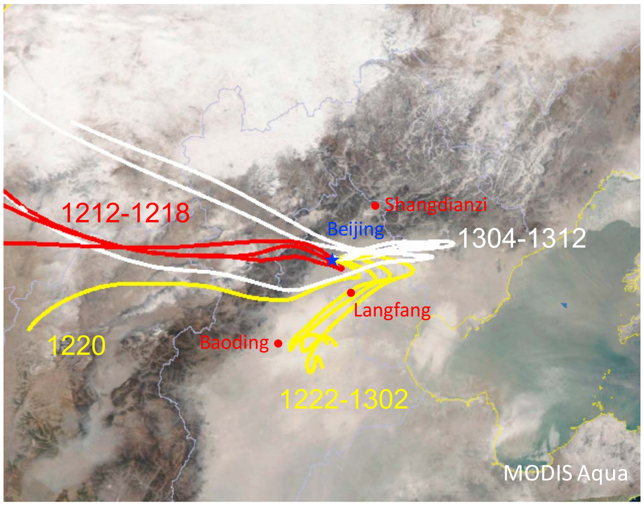

Figure 2. Two day back trajectories arriving at IAP, Beijing between 12:00 on 12 January and 12:00 on 13 January. The back trajectories at 500 m height were calculated every 2 h using NOAA HYSPLIT 4.8 model [*Draxler and Rolph*, 2013]. The numbers indicate the day and time (ddhh) of the trajectories. The two cities of Baoding and Langfang in the Hebei province and a background site Shangdianzi in Beijing are also shown for reference.

was decreased to below 1 km (Figure S8). On the day of 12 January, central eastern China was controlled by a low-pressure system (Figure S9), and in Beijing, a strong temperature inversion with the height exceeding 600 m was observed [*Wang et al.*, 2014a]. These results together suggest that the stagnant synoptic conditions played essential roles in the formation of the severe haze episode by limiting the dispersion of air pollutants. The back trajectories in Figure 2 further showed that the air masses during the severe haze episode on 12 January originated from southwest of Beijing and passed through Baoding and Langfang, two heavily polluted cities in the Hebei province. Consistently, the temporal variations of $PM_{2.5}$ showed peak values in an order of Baoding → Beijing → Shangdianzi (a regional site located to the northeast of Beijing, Figure 2) [*Wang et al.*, 2014b]. The results shown above suggest that regional transport might have also played an important role in the formation of the haze episodes.

Overall, the average (± 1σ) mass concentration of PM_1 for the entire study is 83 (±80) $\mu g\ m^{-3}$ with organics being the major fraction, accounting for 46% (Table 1). The secondary inorganic species ($SO_4^{2-} + NO_3^{-} + NH_4^{+}$) together accounts for 44% of PM_1 with sulfate and nitrate contributing 18% and 15%, respectively. Compared to the same period in January 2012 (Table 1), the concentration of NR-PM_1 shows an increase of ~40% from 60 to 83 $\mu g\ m^{-3}$, indicating worse PM pollution in January 2013. Chloride accounts for a minor faction of PM_1 (3%), which is lower than that observed in January 2012. Because a large fraction of chloride is from coal combustion during wintertime, results here might suggest less coal combustion contribution in this January. Consistently, a decrease of CCOA from 2012 to 2013 was also observed (see section 3.4.3 for details). The average black carbon (BC) concentration is 6.0 $\mu g\ m^{-3}$ for the entire study, which is close to that (6.7 $\mu g\ m^{-3}$) observed previously in winter in Beijing [*Han et al.*, 2009]. BC constitutes a considerable fraction of PM_1, on average accounting for 7%.

3.2. Chemical Evolution of the Record-breaking Haze Episode

The chemical evolution of the long and heavily PM-polluted episode during 10–14 January is shown in Figure 3. The 5 day severe haze evolution is complex involving different meteorological conditions, sources (local versus regional transport), and aerosol processing (photochemical processing and aqueous-phase production). Overall, the haze episode can be classified into four stages (Ep1, Ep2, Ep3, and Ep4 in Figure 3a) with two short periods of clean episodes occurring between. The average mass concentration of PM_1 is 300 (± 129) $\mu g\ m^{-3}$ during the severest haze episode (Ep3), which is 20 times higher than that during the clean period (14 $\mu g\ m^{-3}$) (Table 1). The average PM_1 concentrations varied from 144 to 158 $\mu g\ m^{-3}$ during the other three episodes, which are also increased by a factor of more than 10 compared to the clean period (Figure 3c). The PM levels during the four haze episodes are significantly higher than those observed previously in summer in Beijing by the AMS [*Huang et al.*, 2010; *Sun et al.*, 2010, 2012] and also much higher than the China NAAQS of $PM_{2.5}$ (75 $\mu g\ m^{-3}$, 24 h average).

Figure 3a also shows the average chemical composition of PM_1 for each episode. Overall, the elevated contributions of inorganic species and a corresponding decrease of organics were observed during the haze episodes. For example, when organics decreased from 59% during the clean period to 43–50% during the

Table 1. A Summary of the Average Meteorological Parameters, Mass Concentrations of PM_1 Species and OA Components, and Gaseous Species for the Entire Study, and the Clean Period and the Four Haze Episodes Marked in Figure 1[a]

	Entire Study	Clean	Ep1	Ep2	Ep3	Ep4	January 2012[b]
Meteorological Parameters							
WS ($m\ s^{-1}$)	3.32	4.82	2.17	1.46	1.91	2.10	1.23
Temp (°C)	−5.06	−5.73	−4.35	−2.07	−3.14	−2.84	−2.00
RH (%)	43.7	25.6	70.2	59.7	74.5	70.3	40.1
PM_1 Species ($\mu g\ m^{-3}$)							
Org	38.3	8.2	63.7	78.9	133.6	57.0	31.2
$SO_4{}^{2-}$	14.3	1.2	30.6	24.8	65.3	32.0	8.3
$NO_3{}^{-}$	12.5	1.5	22.0	19.5	40.2	23.1	9.5
$NH_4{}^{+}$	9.2	1.3	18.2	15.4	31.5	17.5	8.1
Chl	2.6	0.4	4.0	3.7	9.3	4.4	3.2
BC	6.0	1.3	11.2	16.0	19.7	9.9	—
PM_1	83.0	13.8	149.8	158.3	299.5	143.9	60.2[c]
OA ($\mu g\ m^{-3}$)							
HOA	5.3	1.5	10.2	8.7	4.2	4.5	5.8
COA	4.8	1.8	4.5	22.7	18.4	3.9	5.5
CCOA	7.3	0.4	13.1	15.9	43.6	15.0	9.1
LSOA	7.8	0.9	12.8	6.0	15.4	7.6	10.8[d]
SV-OOA	8.9	1.3	21.9	25.0	18.7	19.4	
RSOA	4.7	2.3	2.7	1.4	35.0	7.2	
Gases (ppb)							
CO (ppm)	1.7	0.4	2.7	4.1	5.9	3.7	1.9
SO_2	28.9	13.1	51.4	32.5	53.4	44.7	27.6
NO	58.5	16.0	92.3	223.6	144.8	94.9	63.2
NO_2	46.3	27.9	64.3	74.5	90.3	61.0	—
O_3	5.7	11.8	1.2	1.3	1.0	1.0	5.2

[a] The average data during the same period in January 2012 is also shown.
[b] 1–16 January 2012 [*Sun et al.*, 2013b].
[c] PM_1 without BC.
[d] OOA.

four haze episodes, the total inorganic species (= $SO_4{}^{2-} + NO_3{}^{-} + NH_4{}^{+}$ + Chl) were correspondingly elevated from 31% to 40–54%, of which sulfate presented the largest increase from 9% to 16–22%. BC, however, showed similar contributions between clean and haze episodes varying from 7 to 10%. The results shown above suggested an enhanced role of secondary inorganic species in the formation of the haze episodes.

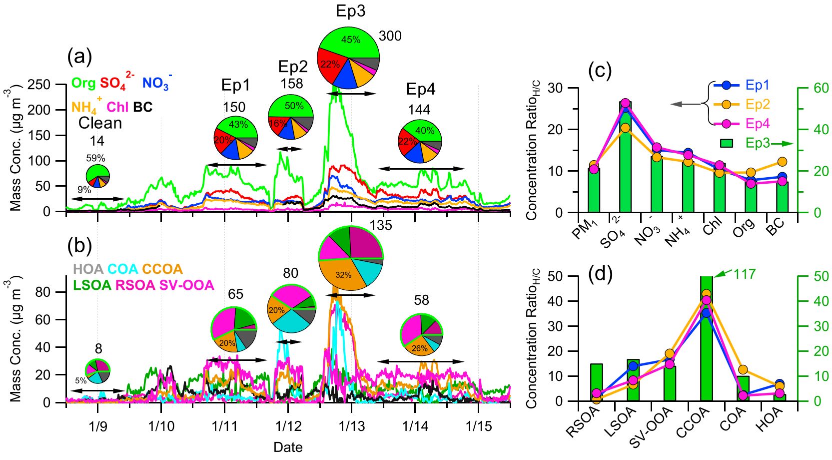

Figure 3. Average chemical composition of (a) PM_1 and (b) organic aerosol during the clean period and the four haze episodes marked in Figure 1. The numbers on the top of the pie charts are the average mass concentrations of PM_1 and OA for each episode. (c and d) The concentration ratios of submicron aerosol species and OA components between the four haze episodes and the clean period.

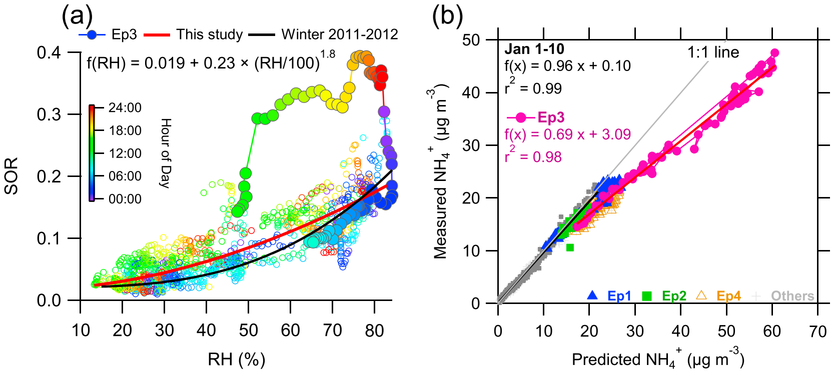

Figure 4. (a) Sulfur oxidation ratio (SOR) as a function of RH. The power fitting line of SOR versus RH during wintertime 2011–2012 is also shown [*Sun et al.*, 2013a]; (b) Correlation between measured NH_4^+ and predicted NH_4^+ (=18 × (2 × SO_4^{2-} / 96 + NO_3^- / 62 + Chl / 35.5)). The regression slopes during 1–10 January and Ep3 are shown.

All submicron aerosol species were substantially increased during the four haze episodes (Table 1). As shown in Figure 3c, the concentration ratios of aerosol species between the haze episodes and the clean period ($R_{H/C}$) varied differently but generally decreased in an order of $SO_4^{2-} > NO_3^- > NH_4^+ > \mathrm{Chl} > \mathrm{BC} > \mathrm{Org}$. Sulfate showed the largest increase among all species, 54 times during Ep3 and 20–26 times during the other three episodes. As shown in Figure 3a, sulfate can quickly exceed nitrate as the major inorganic species of PM_1 during the haze episodes, which is likely due to the aqueous-phase processing associated with increased RH. This is further supported by the much lower $R_{H/C}$ of SO_2 (2.5–4.1) compared to SO_4^{2-} likely indicating that most of the SO_2 was oxidized during the haze episodes. Our previous study during wintertime in Beijing showed that aqueous-phase processing, mostly fog processing, could contribute more than 50% of sulfate production at high RH levels, consistent with higher sulfur oxidation ratios (SOR, molar fraction of sulfate in total sulfur, i.e., sulfate + SO_2) at higher RH levels [*Sun et al.*, 2013a]. The relationship between SOR and relative humidity is presented in Figure 4a. Similar to that observed in *Sun et al.* [2013a], SOR shows a rapid increase as a function of RH, and such correlations are also similar among different wind sectors (Figure S10). The SOR varied from ~0.05 at RH < ~40% to 0.2 at RH = ~80%. In particular, the SOR was greatly increased during Ep3 with the highest value close to 0.4, indicating a large fraction of SO_2 had been oxidized via aqueous-phase processing during this period. The increase of SOR during the haze episodes in winter was also observed by other studies [*Sun et al.*, 2006; *Zhao et al.*, 2013]. Aqueous-phase oxidation of SO_2 to sulfate often leads to an increase of particle acidity. Figure 4b shows the correlation of measured NH_4^+ with predicted NH_4^+ that is needed to fully neutralize sulfate, nitrate, and chloride, i.e., predicted $NH_4^+ = 18 \times (2 \times [SO_4^{2-}] / 96 + [NO_3^-] / 62 + [\mathrm{Chl}] / 35.5)$. A slope of less than 1 indicates acidic aerosol particles, and lower slopes suggest higher acidities [*Zhang et al.*, 2007]. While aerosol particles were overall neutralized before 10 January, they exhibited acidic properties during the four haze episodes (Figure 1d and Figure 4b). The slope of measured versus predicted NH_4^+ is 0.69 during Ep3, indicating highly acidic aerosol particles during this episode. If assuming that the deficiency of NH_4^+ was completely caused by SO_4^{2-}, we estimate that ~60% of SO_4^{2-} existed in the form of ammonium bisulfate (NH_4HSO_4) with the rest being ammonium sulfate ($(NH_4)_2SO_4$) during Ep3. The formation of acidic aerosol particles because of the oxidation of SO_2 to sulfate was also observed during the foggy days [*Kaul et al.*, 2011]. Compared to SO_4^{2-}, NO_3^- presented a lower $R_{H/C}$ likely due to weaker aqueous-phase production associated with lower nitrogen oxidation ratios (Figure S11).

The time series of extinction coefficient is shown in Figure 1d. The average extinction coefficient during the severest haze Ep3 is 2318 $\mathrm{M\,m^{-1}}$, which is more than 60 times higher than that (36.5 $\mathrm{M\,m^{-1}}$) during the clean period. The average extinction coefficient during Ep4 (no available extinction data during Ep2) was also increased by a factor of more than 20 compared to the clean period. The extinction coefficient correlated tightly with $PM_{2.5}$ during 1–10 January ($r^2 = 0.97$, Figure 5), indicating that the light extinction was primarily caused by fine particles. The mass extinction efficiency (MEE) obtained from the linear regression analysis is 2.7 $\mathrm{m^2\,g^{-1}}$, which is overall in agreement with the values reported previously in Beijing [*Garland et al.*, 2008; *Jung et al.*, 2009]. While tight correlations between extinction and $PM_{2.5}$ existed during Ep3 and Ep4, higher

MEE (~ 4.1 $m^2 g^{-1}$) was observed in comparison to that before 10 January. The enhanced MEE during the haze episodes was likely associated with the change of aerosol composition and size distributions. For example, the PM_1 composition during Ep3 and Ep4 showed higher contributions of ammonium nitrate and ammonium sulfate and lower fraction of organics compared to the period of 1–10 January. *Jung et al.* [2009] also found a large increase of mass scattering efficiency from clean periods (2.0 $m^2 g^{-1}$) to relatively polluted conditions (4.1 $m^2 g^{-1}$) in Beijing. It should be noted that the MEE at 630 nm would be increased by ~30% if it is converted to that at 532 nm using an extinction angstrom exponent of 1.4 [*Pereira et al.*, 2011].

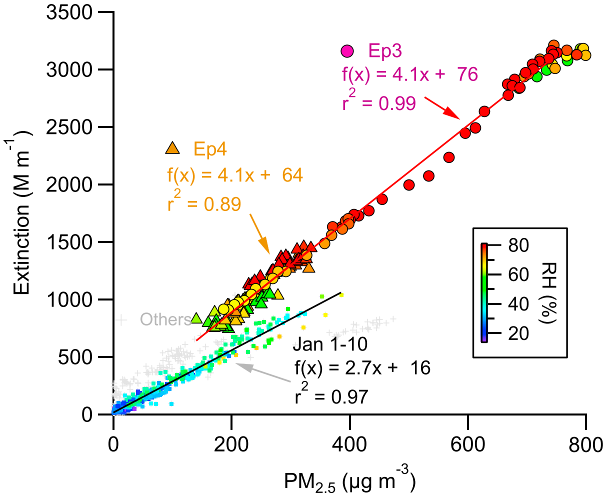

Figure 5. Correlation between particle extinction and $PM_{2.5}$. The data points are color coded by RH.

3.3. Vertical Profiles

Figure 6a shows the vertical evolution of backscattering coefficients (BSC) and the variations of boundary layer height (BLH) during 9–15 January. Higher BSC values were observed at lower heights than BLH suggesting that the haze pollution was predominantly formed and evolved inside boundary layer. The BLH was generally < 1 km and was as low as 300 m at night during the four haze episodes. The shallow boundary layer limited the vertical dispersions of air pollutants and facilitated the formation of the haze episodes. Figure 6b shows a comparison of the PM_1 measured at the ground site with the BSC at the height of 240 m. The PM_1 was tightly correlated with BSC before 10 January ($r^2 = 0.86$) suggesting that the air pollutants below 240 m were well mixed before the severe haze episodes. However, the PM_1 did not correlate much with BSC during the four haze episodes, and the ratios of PM_1 to BSC were overall higher than those during 1–10 January. One of the reasons was likely due to the strong, yet not uniform vertical gradients of BSC. Indeed, the BSC showed strong vertical gradients within boundary layer that were characterized by rapid decreases as a function of height (Figure 7a). Also note that the ratios of BSC between the haze episodes and the clean period were much higher at low heights (e.g., < 400 m) confirming that the air pollutants during the haze episodes were concentrated at low heights because of the shallow boundary layer.

Figures 7b–7d show the average vertical profiles of meteorological parameters (RH, temperature, and wind speed) during the four haze episodes and the clean period. The three haze episodes of Ep1, Ep3, and Ep4 showed similar vertical profiles of meteorological parameters. The RH remained consistently high at ~70% with minor variations across different heights. The temperature was < 0 °C and decreased as a function of height. The wind speed was ~ 1 m s^{-1} at low heights and showed an increase of ~ 1 m s^{-1} at high heights. These results suggest the similar and consistently stagnant meteorological conditions below 320 m during

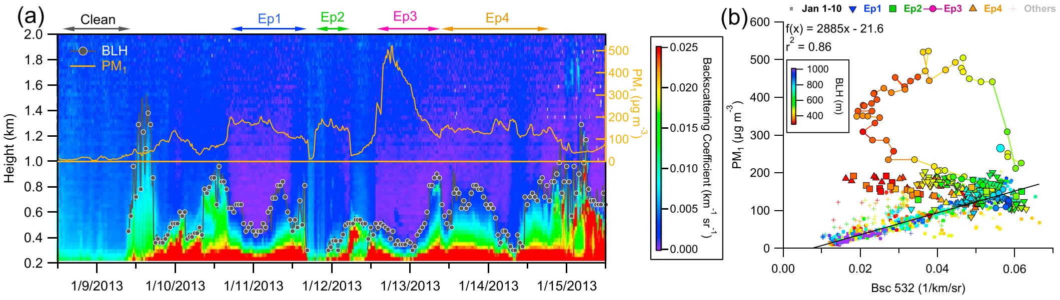

Figure 6. (a) Vertical evolution of backscattering coefficient (532 nm) and temporal variations of boundary layer height (BLH) and PM_1. (b) Correlation of PM_1 versus backscattering coefficient (Bsc) with the data segregated into four haze episodes.

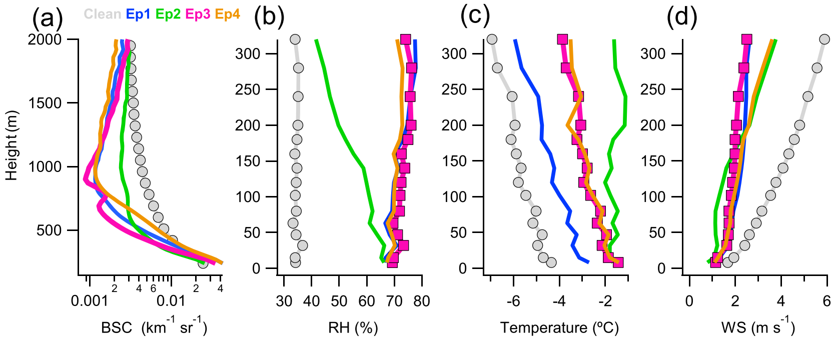

Figure 7. Average vertical profiles of (a) backscattering coefficient (BSC), (b) relative humidity (RH), (c) temperature, and (d) wind speed (WS) during the clean and four haze episodes.

these three haze episodes. As a result, the aerosol particles showed similar compositions with organics being the major fraction (40–45%) followed by sulfate (20–22%), nitrate (13–16%), ammonium (10–12%), and BC (~7%). The vertical profiles of meteorological parameters during Ep2 were different. The RH decreased as a function of height from ~70% to ~40%, and the temperature showed a small inversion between ~200 and 250 m. The vertical evolution of meteorological conditions (not shown in this study) showed persistently low RH and prevalent northerly winds at high heights during Ep2. However, there was a wind direction change from the north to the south at low heights (< 100 m), while the meteorological conditions remained stagnant (high RH and low WS). As shown in Figure 3a, the haze in Ep2 was formed in less than 1 h (18:00–19:00) during which the mass concentrations of inorganic species were quickly elevated to similar levels observed during Ep1. It is very likely that the northern air masses clearing out Ep1 still dominated the high heights, whereas the southern air masses had replaced those at low heights during the formation of Ep2.

3.4. Investigation of OA Composition and Sources

PMF analysis of ACSM OA mass spectra resolved six OA factors including three POA factors, i.e., hydrocarbon-like OA (HOA), cooking OA (COA), and coal combustion OA (CCOA), and three SOA factors, i.e., regional SOA (RSOA), semivolatile oxygenated OA (SV-OOA), and local SOA (LSOA). Compared to the previous four-factor solution during wintertime 2011–2012 [*Sun et al.*, 2013b], this study was able to resolve two more secondary factors while the other three POA factors are similar. The increased number of PMF factors

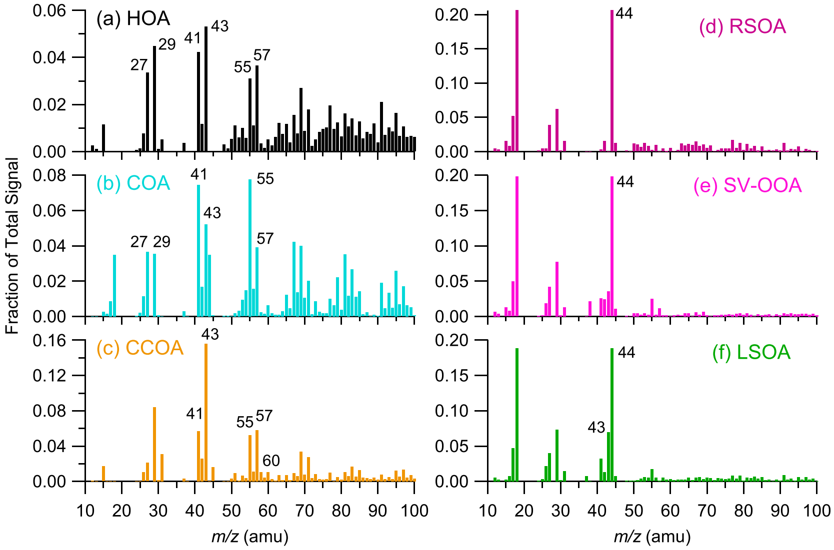

Figure 8. Mass spectra of the six OA components for the entire study: (a) HOA, (b) COA, (c) CCOA, (d) RSOA, (e) SV-OOA, and (f) LSOA.

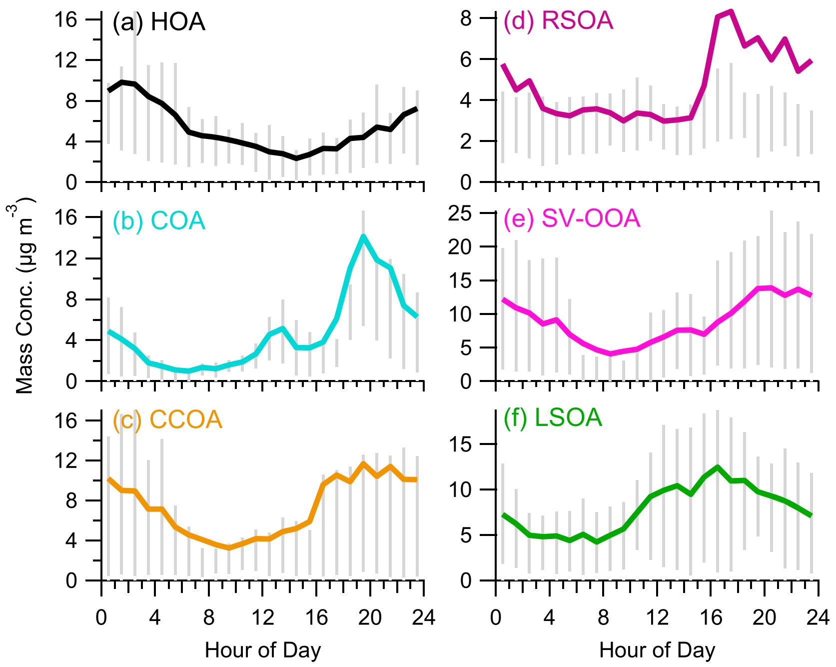

Figure 9. Diurnal cycles of the six OA components for the entire study: (a) HOA, (b) COA, (c) CCOA, (d) RSOA, (e) SV-OOA, and (f) LSOA. The gray sticks refer to 25th and 75th percentiles.

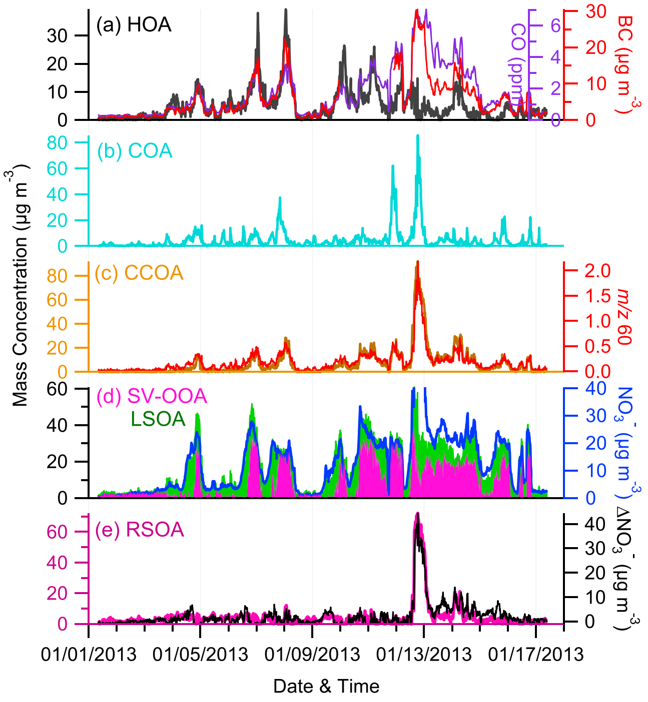

Figure 10. Time series of the six OA components: (a) HOA, (b) COA, (c) CCOA, (d) SV-OOA and LSOA, and (e) RSOA. Also shown are the corresponding tracer species, including BC, CO, *m/z* 60, and NO_3^-. SV-OOA and LSOA are stacked in Figure 10d. The ΔNO_3^- in Figure 10e is calculated by equation (2).

was likely due to the more complex OA sources in this specific January. In addition, the previous OOA appeared to be split into SV-OOA and LSOA that showed different time series and diurnal variations yet can be reasonably explained by different formation mechanisms. The mass spectra, diurnal profiles, and time series of the six OA components are shown in Figures 8–10.

3.4.1. Hydrocarbon-Like OA

Similar to the previously reported HOA spectra [*Zhang et al.*, 2005b; *Ng et al.*, 2011a] and the source spectra of diesel fuels [*Canagaratna et al.*, 2004], the HOA spectrum in this study is characterized by prominent hydrocarbon ion series of $C_nH_{2n-1}^+$ and $C_nH_{2n+1}^+$ (Figure 8a). The HOA spectrum also resembles that resolved during wintertime 2011–2012 ($r^2 = 0.79$, Figure S7a) [*Sun et al.*, 2013b], yet the ratios of $C_nH_{2n-1}^+$/$C_nH_{2n+1}^+$ (e.g., *m/z* 27/29, *m/z* 41/43, and *m/z* 55/57) have some differences and the reasons are not clear yet. The

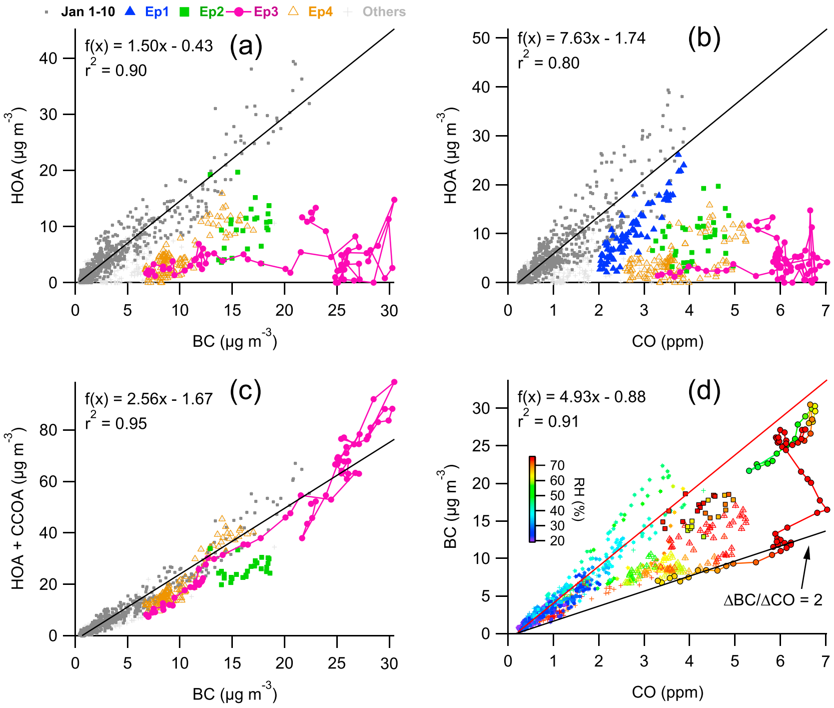

Figure 11. Correlations of (a) HOA versus BC, (b) HOA versus CO, (c) HOA + CCOA versus BC, and (d) BC versus CO. The data are segregated into the four haze episodes that are marked in Figure 1. The correlations with regression coefficients during 1–10 January are also shown for comparison.

HOA presents a pronounced diurnal cycle with high concentration occurring at night (Figure 9a), similar to that in winter 2011–2012 [*Sun et al.*, 2013b]. The highest concentration of HOA (~10 μg m^{-3}) occurred between 1:00 and 3:00 when HOA accounted for ~25% of OA. The HOA then decreased gradually during daytime and reached a minimum of 2.3 μg m^{-3} (7% of OA) at 14:00–15:00. The diurnal cycle of HOA was likely driven by the number of diesel trucks and heavy-duty vehicles that showed remarkably similar diurnal pattern [*Han et al.*, 2009] although the variation of BLH also played a role (Figure S12a).

The HOA on average accounted for 14% of OA for the entire study, which is overall consistent with the values previously reported in Beijing [*Huang et al.*, 2010; *Sun et al.*, 2013b]. While the HOA concentration was increased by a factor of 3–7 during the four haze episodes compared to the clean period, the contribution of HOA to OA decreased instead. In particular, HOA only accounted for 3% of OA during the record-breaking haze episode (Ep3) and also less than 10% during Ep4. These results indicate that the traffic emissions from diesel trucks and heavy-duty vehicles were likely not significant contributors to the severe haze Ep3 and Ep4. Consistently, many highways were closed because of the low visibilities ($<$ 1 km, Figure S8) and heavy fog during the two episodes. As a result, the number of diesel trucks and heavy-duty vehicles on the road were expected to be much less than other periods.

The HOA correlates well with the primary combustion tracers of BC ($r^2 = 0.90$, Figure 11a) and CO ($r^2 = 0.80$, Figure 11b) before the four haze episodes. The average ratio of HOA/BC (1.5) is close to that observed in Pittsburgh [*Zhang et al.*, 2005a], Mexico City [*Aiken et al.*, 2009], and New York City [*Sun et al.*, 2011] and also that observed in Pasadena, California, during periods with more emissions from diesel trucks than gasoline vehicles [*Hayes et al.*, 2013]. The ratio of HOA/CO (7.6) is also close to that observed in Pasadena, California (6.4) [*Hayes et al.*, 2013], and Fresno, California (5.6) [*Ge et al.*, 2012]. Compare to the period of 1–10 January, the HOA shows different correlations with BC and CO and also much lower ratios of HOA/BC and HOA/CO during the four haze episodes indicating different sources between haze and nonhaze episodes. However, the total of HOA and CCOA correlates tightly with BC ($r^2 = 0.95$, Figure 11c), and no significant differences were observed between haze episodes and other periods. These results suggest that CCOA is also a significant contributor to BC during haze episodes [*Chen et al.*, 2009]. Although the correlation of HOA versus CO was improved after considering CCOA, the lower ratios of HOA + CCOA to CO were still observed during the haze episodes (Figure S13), likely indicating different sources and/or processes of CO compared to aerosol particle species. It is interesting to compare the correlation of the two combustion tracers, BC and CO. The BC was highly correlated with CO before the four haze episodes ($r^2 = 0.91$, Figure 11d) and the regression slope (4.93) fell within the range of seasonal averages of ΔBC/ΔCO (3.5–5.8) observed in Beijing [*Han et al*., 2009]. However, lower ratios of BC/CO were observed during the four haze episodes. Similar low ratios of ΔBC/ΔCO during wintertime owing to the enhanced CO emissions from coal combustion were also observed previously in Beijing [*Han et al*., 2009]. Therefore, the low BC/CO ratios during the haze episodes were likely due to the influences of coal combustion emissions that were characterized by lower BC/CO ratios compared to other sources. For example, as the contribution of CCOA to OA was increased from ~10% to >30% during Ep3 in half a day, the BC/CO ratio evolved quickly from 4.8 to ~2.0. The low ratios of BC/CO might also be due to the high liquid water content during the foggy periods which scavenged BC more efficiently than gaseous CO [*Pan et al*., 2011]. Correspondingly, the correlation of BC versus CO was strongly RH dependent with lower ratios associated with higher RH levels (Figure 11d).

3.4.2. Cooking OA

The AMS-resolved COA shows a distinct mass spectral profile which is characterized by prominent *m/z* 55 ($C_4H_7^+$, $C_3H_3O^+$) and *m/z* 57 ($C_4H_9^+$, $C_3H_5O^+$), and a higher ratio of *m/z* 55/57 (= 2) than the other two primary OA components (= ~1). The COA spectrum is also similar to that resolved in winter 2011–2012 ($r^2 = 0.90$, Figure S7b) [*Sun et al*., 2013b]. The COA presents a pronounced diurnal cycle with two obvious peaks appearing at lunch and dinner time (Figure 9b). The COA concentration reached a maximum of 14 $\mu g\ m^{-3}$ between 19:00 and 20:00 and then quickly dropped to the lowest value of ~1 $\mu g\ m^{-3}$ in early morning. Similar diurnal behaviors of COA have been observed in Beijing and other urban sites [*Allan et al*., 2010; *Huang et al*., 2010; *Sun et al*., 2011, 2013b].

COA on average accounted for 12% of OA for the entire study, which was lower than those (~20%) observed in both summer and winter in Beijing [*Huang et al*., 2010; *Sun et al*., 2013b; *Zhang et al*., 2013a], yet the contribution of COA during the clean period (22%) was comparable. The COA varied dramatically throughout the study. Compared to the clean period, the COA was elevated by more than 10 times during Ep2 and Ep3, but only a factor of ~2 during Ep1 and Ep4 (Figure 3d). Correspondingly, the contributions of COA to OA during Ep2 and Ep3 (28% and 14%, respectively) were higher than those during the other two episodes (~7%). As shown in Figure 10b, the COA presents two pronounced peaks during Ep2 and Ep3 with the peak concentration approaching 90 $\mu g\ m^{-3}$. The two peaks coincidently happened on Friday and Saturday nights when enhanced cooking activities were expected. However, similar COA peaks were not observed during the other two episodes. Given the considerable contribution of COA to OA, reducing cooking activities would help mitigate the PM pollution during the haze episodes.

3.4.3. Coal combustion OA

A CCOA factor was resolved in this study, which shows a similar spectral pattern to that in winter 2011–2012 ($r^2 = 0.82$, Figure S7c) [*Sun et al*., 2013b] and also that identified by a high-resolution AMS at a rural site in central eastern China [*Hu et al*., 2013]. The CCOA spectrum resolved in *Hu et al*. [2013] shows typical fragment patterns of polycyclic aromatic hydrocarbons (PAHs) at *m/z* > 120, which cannot be seen in our study because of the limited ion transmission efficiency of the ACSM [*Ng et al*., 2011b]. Further support for the presence of CCOA is its tight correlation with two combustion tracers, i.e., *m/z* 60 ($r^2 = 0.93$, Figure 10c) and chloride ($r^2 = 0.83$). The CCOA shows a pronounced diurnal cycle with the nighttime concentration approximately 2 times higher than that observed during daytime. This is consistent with the enhanced emissions of coal burning for heating at night. The CCOA on average accounts for 19% of OA for the entire study, which is lower than 29% in January 2012 [*Sun et al*., 2013b]. Also, the average mass concentration of 7.3 $\mu g\ m^{-3}$ is lower than 9.1 $\mu g\ m^{-3}$ during the same period of January 2012 (Table 1). The variations of CCOA as a function of RH in 2012 and 2013 are compared in Figure S14. If not considering Ep3 with large contributions from regional transport (section 3.5), the average mass concentration of CCOA and its contribution to OA in January 2013 are ubiquitously lower than those in January 2012 across different RH levels (Figure S14). Even when considering Ep3, the CCOA concentration is also lower in 2013 compared to 2012 except at two RH levels (50–60% and > 80%). These results might indicate that coal combustion emissions were reduced due to the gradual replacement of coal-fired boilers by natural gas boilers in Beijing (http://www.bjepb.gov.cn/bjepb/323474/324034/324735/index.html).

The CCOA contributed a minor fraction of OA (5%) during the clean period with an average concentration of less than 1 $\mu g\,m^{-3}$. However, the CCOA concentration was increased by more than 30 times during the four haze episodes (Figure 3d). Correspondingly, the contribution of CCOA to OA exceeded 20% during all haze episodes (Figure 3b and Table 1). Among the six OA factors, CCOA showed the largest increase during the severest haze Ep3 with the peak concentration exceeding 80 $\mu g\,m^{-3}$ (Figure 3b). The average contribution of CCOA to OA was also increased to 32% during Ep3. High concentrations of CCOA during the four haze episodes were likely caused by both stagnant meteorological conditions and high RH ($>$ 60%) that facilitates the partitioning of water-soluble organic compounds from coal combustion emissions into the aqueous phase. Indeed, CCOA is the only OA factor with its contribution to OA increasing as a function of relative humidity [*Sun et al.*, 2013a]. Despite this, further investigations are needed to have a full understanding of the phase partitioning of CCOA during wintertime.

3.4.4. Secondary Organic Aerosol

A highly oxidized secondary OA from regional transport (RSOA) with the spectrum resembling that of fulvic acid [*Zhang et al.*, 2005b] was identified first in Beijing (Figure 8d). The RSOA correlates well with the NO_3^- from regional transport (ΔNO_3^-, see below for detail) ($r^2 = 0.86$, Figure 10e) confirming the presence of RSOA. The time series of RSOA varied differently from the other SOA factors, which was characterized by a large peak during Ep3 (Figure 3b) and relatively high concentration during Ep4 (Table 1). Compared to the clean period, the RSOA concentration was increased by a factor of 15 and 3 during Ep3 and Ep4, respectively. The contribution of RSOA to OA was also increased from $<$5% during the first two haze episodes (Ep1 and Ep2) to 26% and 13% during Ep3 and Ep4, respectively.

The two SOA factors (SV-OOA and LSOA) show similar spectral patterns, yet their time variations and diurnal cycles differ greatly (Figures 8–10). The SV-OOA shows a pronounced diurnal cycle with lower concentration during daytime and higher concentration at night (Figure 9e). Such a diurnal variation is similar to that of RH yet opposite to that of temperature. Therefore, SV-OOA is likely an OA factor driven by gas-particle partitioning associated with RH and temperature. Given the low temperature ($<$ 3.3 °C) in this study, the phase partitioning of semivolatile organic compounds associated with RH [*Hennigan et al.*, 2008] might have played a major role in the formation of SV-OOA. This is further supported by the relatively constant SV-OOA during the haze episodes when the RH variations are not significant. Compared to SV-OOA, the diurnal cycle of LSOA presents a gradual increase from ~5 $\mu g\,m^{-3}$ at ~8:00 to 12.5 $\mu g\,m^{-3}$ at 17:00 (Figure 9f), indicating photochemical production of LSOA during daytime. Such a diurnal cycle is similar to that of OOA during wintertime 2011–2012 [*Sun et al.*, 2013b]. The LSOA on average accounted for 20% of OA for the entire study with the highest contribution of approximately 30% in the early afternoon. The contribution of LSOA varied among different episodes ranging from 8% to 20%. As a comparison, the contribution of SV-OOA to OA shows a large increase from 16% during the clean period to more than 30% during the other three haze episodes except Ep3 (Table 1). One explanation is that the largely increased CCOA and RSOA during Ep3 led to a decrease of relative contribution of SV-OOA. We also noticed that the evolution of LSOA and SV-OOA appeared to be intrinsically linked. Figure 3b shows that the decrease of LSOA coincidently corresponded to an increase of SV-OOA, which likely indicated a transformation of newly formed SOA on preexisting particles via phase partitioning [*Williams et al.*, 2010].

The total of SV-OOA and LSOA (SLOA) correlates tightly with NO_3^- ($r^2 = 0.92$, Figure 12a) during 1–10 January, whereas the ratio of NO_3^-/SLOA (0.62) is lower than that observed in winter 2011–2012 [*Sun et al.*, 2013b]. It appears that SV-OOA and LSOA represent two formation mechanisms of SOA, i.e., gas-particle partitioning and photochemical production, both of which play important roles in the formation of nitrate. It should be noted that NO_3^- correlates better with LSOA ($r^2 = 0.62$) compared to SV-OOA ($r^2 = 0.49$), suggesting that photochemical processing plays a more important role than phase partitioning in the formation of NO_3^- during wintertime. Compared to the other periods, NO_3^- correlates weakly with SLOA ($r^2 = 0.41$) and presents higher NO_3^-/SLOA ratios during Ep3 (Figure 12a). NO_3^-, however, correlates tightly with the total SOA (= SV-OOA + LSOA + RSOA) ($r^2 = 0.94$, Figure 12b) suggesting that part of NO_3^- during Ep3 was closely

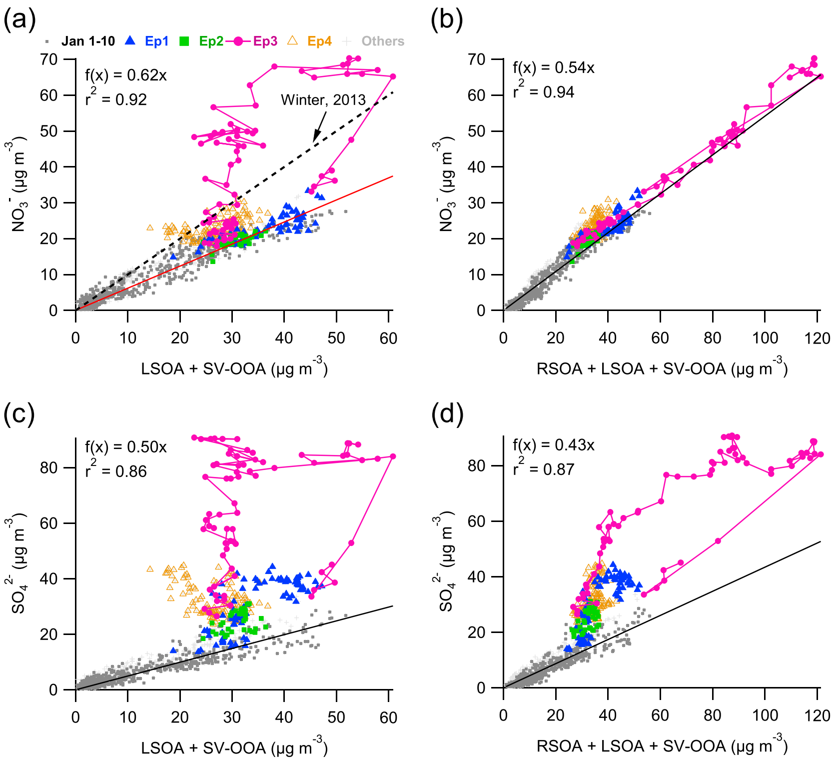

Figure 12. Correlations of (a) NO_3^- versus LSOA + SV-OOA, (b) NO_3^- versus RSOA + LSOA + SV-OOA, (c) SO_4^{2-} versus LSOA + SV-OOA, and (d) SO_4^{2-} versus RSOA + LSOA + SV-OOA. The data are segregated into four haze episodes that are marked in Figure 1. The correlations with regression coefficients during 1–10 January are also shown for comparison.

related to RSOA. Given that RSOA is a factor from regional transport, the RSOA-related NO_3^- during Ep3 is also expected to be from regional transport. Assuming that the SLOA-related NO_3^- is predominantly from local production, the regional-transported NO_3^- can be estimated as

$$\Delta[NO_3^-] = [NO_3^-]_{Total} - [SLOA] \times ([NO_3^-]/[SLOA])_{Local} \tag{2}$$

where $\Delta[NO_3^-]$ is the NO_3^- from regional transport, $[NO_3^-]_{Total}$ is the total NO_3^-, and $([NO_3^-]/[SLOA])_{Local}$ is the ratio of NO_3^- to SLOA from local sources which is 0.62 in this study (Figure 12a). As shown in Figure 10e, $\Delta[NO_3^-]$ shows a similar time trend compared to RSOA ($r^2 = 0.86$), suggesting similar sources of $\Delta[NO_3^-]$ and LSOA, i.e., regional transport. The average $\Delta[NO_3^-]$ concentration during Ep3 is 19.1 $\mu g\ m^{-3}$, accounting for 48% of total NO_3^-, which suggests that regional transport on average contributed half of NO_3^- during Ep3.

SO_4^{2-} also correlates tightly with SLOA ($r^2 = 0.86$, Figure 12c) and SOA ($r^2 = 0.87$, Figure 12d) during 1–10 January. The average ratio of SO_4^{2-}/SOA (0.43) is close to that (0.41) observed during wintertime 2011–2012 when the RH was less than 30% [*Sun et al.*, 2013a]. As shown in Figure 1b, the RH during 1–10 January was generally below 40% and the aerosol water content predicted by E-AIM model [*Clegg et al.*, 1998] was correspondingly low ($< 0.01\ g\ m^{-3}$). Therefore, aqueous-phase production of sulfate was expected to be low, and hence, sulfate likely shared the same photochemical formation mechanism with SOA. The photochemical production of SOA is also supported by the tight correlation between SOA and O_x ($= O_3 + NO_2$) ($r^2 = 0.88$, Figure 13), a conserved tracer for photochemical processing [*Herndon et al.*, 2008]. In comparison, weaker correlations of SO_4^{2-} versus SOA ($r^2 = 0.14–0.71$) and higher average ratios of SO_4^{2-}/SOA (0.76–0.93) were observed during the four haze episodes (Figure 12d) which indicated the different sources and processes between haze and nonhaze episodes. The higher ratios of SO_4^{2-}/SOA suggested additional sources of sulfate compared to SOA, for example, aqueous-phase processing and/or

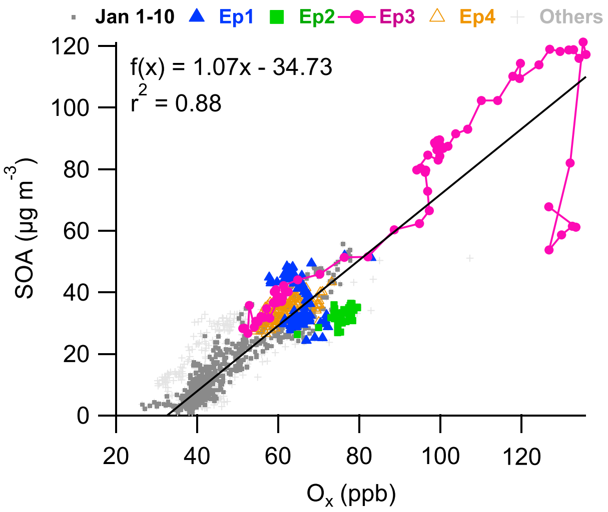

Figure 13. Correlation between SOA (= RSOA + LSOA + SV-OOA) and O_x (= $O_3 + NO_2$). The data are segregated into a clean period and four haze episodes that are marked in Figure 1. The correlation with regression coefficient before 10 January is shown for comparison.

regional transport. If assuming that the SOA during the four haze episodes was predominantly from photochemical processing, we then can estimate the contributions of additional sources to the total sulfate using the following equation:

$$\left[SO_4^{2-}\right]_{NPP} = \left[SO_4^{2-}\right]_{Total} - [SOA] \times \left[SO_4^{2-}/SOA\right]_{NHE} \quad (3)$$

where $[SO_4^{2-}]_{NPP}$ is the sulfate from the sources of nonphotochemical production, $[SO_4^{2-}]_{Total}$ is the total sulfate measured, and $[SO_4^{2-}/SOA]_{NHE}$ is the average ratio of SO_4^{2-}/SOA during nonhaze episode which is 0.43 in this study. With this approach, we estimate that the sulfate not from photochemical production approximately contributed on average 44–54% of the total sulfate during the four haze episodes.

The total SOA constituted a large fraction of OA varying from 41 to 59% during the four haze episodes. On average, SOA accounted for 55% of OA for the entire study, which showed a large increase compared to that (35%) in January 2012 (Table 1). The SOA correlates tightly with odd oxygen (O_x) ($r^2 = 0.88$, Figure 13). However, the slope of SOA versus O_x is 1.07 $\mu g\ m^{-3}\ ppb^{-1}$, which is much higher than those (typically ~100–120 $\mu g\ m^{-3}\ ppm^{-1}$) observed in Mexico City [*Herndon et al.*, 2008; *Aiken et al.*, 2009] and New York City [*Sun et al.*, 2011] in summer. This might indicate a different photochemical processing between summer and winter because of different meteorological conditions and precursors. The O_3 level was consistently low (< 30 ppb) throughout the study and was only a few ppb during the haze episodes (Figure 1), largely due to the titration of O_3 by the high level of NO. The photochemical age calculated from $-\log[NO_x/NO_y]$ is less than 0.1 across the entire study, suggesting fresh air masses during wintertime. The SOA even correlates with NO_x ($r^2 = 0.60$), a tracer for primary traffic emissions. These results together indicate that SOA during wintertime is relatively fresh, consistent with the freshly aged SOA (oxygen-to-carbon ratio < ~0.4) observed previously during wintertime in Beijing [*Liu*, 2012].

3.5. Regional Contributions During the Record-Breaking Haze Episode (Ep3)

Regional transport has been identified as an important contribution to the haze pollution in Beijing [*Jia et al.*, 2008]. However, to our knowledge, there are no unique tracers that can perfectly distinguish local sources and regional transport. Based on the characteristics of "sawtooth cycles," *Jia et al.* [2008] developed a technique to estimate the regional contributions of $PM_{2.5}$. It was estimated that regional transport on average contributed approximately 50% of PM (up to 70%) during the southerly flow. However, this approach might have large uncertainties without considering the accumulation of local pollutants.

Figure 3a shows that all aerosol species rapidly decreased at ~6:00 and then remained at consistently low levels between 6:00 and 9:00 on 12 January. The lidar data also show an evident uplift of air pollutants to the height of ~600 m and a corresponding clean layer at the height of below 400 m during this period (Figure 6a). After 9:00, all aerosol species started to build up with approximately linear increases, e.g., 17 $\mu g\ m^{-3}\ h^{-1}$ for PM_1. The chemical evolution was interrupted at ~13:30 by a steep increase that was completed in 2.5 h. Such rapid changes could not be finished in such a short period of time if there were only contributions from local sources. Regional transport, however, was likely the major reason for such rapid enhancements. Indeed, the MODIS satellite image in Figure S15 shows an evident regional transport from ~11:00 to ~13:00–14:00 as suggested by the appearance of haze over the mountainous areas where there are almost no local sources. Therefore, the chemical evolution of aerosol species on 12 January can be classified into two different stages. The first stage (~9:00–13:00) was primarily caused by local accumulation, and the second

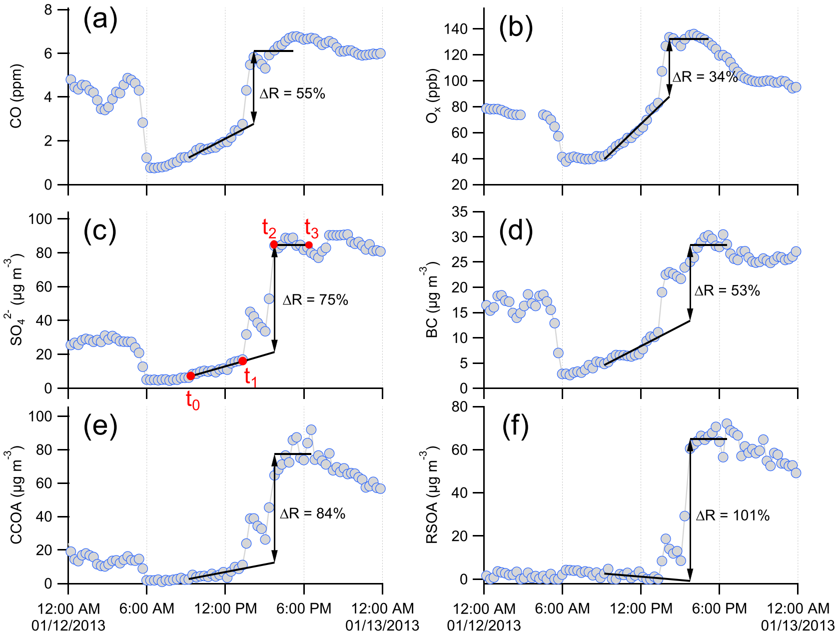

Figure 14. Selected examples for calculation of the regional contributions during Ep3: (a) CO, (b) O_x (= $O_3 + NO_2$), (c) SO_4^{2-}, (d) BC, (e) CCOA, and (f) RSOA. Δ*R* refers to the contribution from regional transport.

stage (~13:00–18:30) was predominantly contributed by regional transport. The differences between the two stages are then assumed to be the contributions from regional transport. To calculate the local and background concentrations, we first assume the linear increases of aerosol species from t_0 (~9:00) to t_1 (~13:00) (Figure 14c) and continuous build up are at the same rates until t_2 (~16:00). A linear fit was then performed between t_0 and t_1 for each species (Figure 14c). The regression slope represents the average increasing rate (S in μg m^{-3} h^{-1}), and the intercept (I) is the background concentration of each species. The concentration at t_2 (C_{L+B}) that mixed both local sources (L) and background (B) can be calculated with equation (4):

$$C_{L+B} = I + S \times t_2 \tag{4}$$

Using the average concentration between t_2 to t_3 (18:30) to represent the peak of Ep3 (C_{L+B+R}) that mixed the contributions from background, local sources, and regional transport (R), the regional contributions (ΔR) from t_1 to t_2 can be calculated with equation (5).

$$\Delta R = (C_{L+B+R} - C_{L+B})/C_{L+B+R} \times 100\% \tag{5}$$

Table 2. Estimated Regional Contributions (Δ*R*) to the Selected Species During the Peak Pollution of Ep3 (15:45–18:30)[a]

Species	ΔR	ΔR_O	Gases	ΔR
PM_1	66%		O_x	34%
Org	67%		NO_2	35%
SO_4^{2-}	75%	70%[b]	CO	55%
NO_3^-	55%	53%[b]		
NH_4^+	62%			
Chl	75%			
BC	53%			
SOA	59%	56%[c]		
RSOA	101%			
CCOA	84%			

[a] The regional contributions estimated from other approaches (ΔR_O) are also shown for comparison.

[b] Regional contribution estimated with equation (6).

[c] Fraction of RSOA in SOA assuming RSOA is completely from regional transport.

The estimated regional contributions to selected species are shown in Table 2, and the examples for the calculations are shown in Figure 14. It should be noted that there are also possibilities that the local air masses were partly or completely replaced by the new ones from regional transport during the period of sudden increase ($t_1 \rightarrow t_2$). In this case, the regional transport would contribute more than that estimated with equation (5). Therefore, the estimations in this study represent the lowest limits of regional contributions. This approach is further evaluated by comparing with other methods. As shown in Figures 12a and 12c, SO_4^{2-} and NO_3^- show different correlations with SLOA (SV-OOA + LSOA) during Ep3 in comparison to the period of 1–10 January, particularly the higher ratios of SO_4^{2-}/SLOA and NO_3^-/SLOA. Given that SV-OOA and LSOA were mainly from local production (section 3.4.4), the ratio differences were likely caused primarily by regional transport. We then estimate the regional contributions of SO_4^{2-} and NO_3^- (ΔR_{SN}) during the peak pollution of Ep3 as

$$\Delta R_{\mathrm{SN}} = \left[(\mathrm{SN}/\mathrm{SLOA})_{\mathrm{peak}} - (\mathrm{SN}/\mathrm{SLOA})_{\mathrm{NHE}}\right]/(\mathrm{SN}/\mathrm{SLOA})_{\mathrm{peak}} \times 100\% \tag{6}$$

where SN is SO_4^{2-} or NO_3^-; $(\mathrm{SN/SLOA})_{\mathrm{peak}}$ is the average ratio of SN/SLOA during the peak pollution of Ep3 (16:00–18:30), which is 1.65 and 1.32 for SO_4^{2-}/SLOA and NO_3^-/SLOA, respectively; $(\mathrm{SN/SLOA})_{\mathrm{NHE}}$ is the average ratio of SN/SLOA during 1–10 January, which is 0.50 and 0.62 for SO_4^{2-}/SLOA and NO_3^-/SLOA, respectively. From equation (6), it was estimated that regional transport on average contributed 70% and 53% to SO_4^{2-} and NO_3^-, respectively, which is consistent with that estimated by equation (5) (Table 2). In addition, the regional contribution of RSOA was estimated to be 100%, which is consistent with the fact that RSOA was predominantly from regional transport (section 3.4.4). Further, the calculated regional contribution of SOA (59%) also agrees well with the fraction of RSOA in total SOA (56%). All these results suggest that our approach for estimating regional contributions during Ep3 is rational. We also found that this approach is not applicable for local pollutants such as HOA, COA, and LSOA because they did not exhibit the similar behavior of a sudden increase.

The regional transport on average contributed 66% to PM_1 suggesting that the severest haze Ep3 was primarily caused by regional transport. The regional transport also contributed a large fraction of submicron aerosol species ranging from 53 to 100% (Table 2). Except RSOA, the regional transport contributed the largest to sulfate and CCOA, accounting for 75% and 84%, respectively. The back trajectories in Figure 2 show that the air masses during Ep3 originated from the most polluted regions south of Beijing, such as Baoding and Langfang in the Hebei province, where lots of coal power plants are located [*Kurokawa et al.*, 2013]. On the day of 12 January, the mass concentration of $PM_{2.5}$ at Baoding exceeded 800 $\mu g\ m^{-3}$ [*Wang et al.*, 2014b]. Not surprisingly, the air masses passing through these highly polluted regions would carry a large amount of pollutants to Beijing, in particular sulfate and CCOA. Compared to aerosol particle species, regional transport appeared to contribute less to gaseous species, for example, 34% and 35% for O_x and NO_2, respectively (Table 2). However, regional transport contributed a higher fraction to CO (55%) compared to O_x and NO_2, which was likely due to more CO emissions associated with coal combustion.

4. Conclusions

We have a comprehensive characterization of the sources and chemical evolution of severe haze pollution that occurred in Beijing in January 2013. Four haze episodes were observed during 10–14 January with the average PM_1 mass concentrations ranging from 144 to 300 $\mu g\ m^{-3}$. In particular, a record-breaking haze episode (Ep3) with the peak concentration exceeding 500 $\mu g\ m^{-3}$ occurred on 12 January. All submicron aerosol species were substantially elevated during the four haze episodes, among which sulfate and coal combustion organic aerosol presented the largest increase. Compared to the clean period, the four haze episodes showed elevated contributions of secondary inorganic species and a corresponding decrease of organics indicating the enhanced roles of secondary inorganic species in the formation of haze episodes. The chemical evolution of aerosol species during the four haze episodes was strongly associated with stagnant meteorological conditions and shallow boundary layers. For example, under high humidity conditions, sulfate concentration often quickly exceeded nitrate due to the rapid aqueous-phase production. The particle extinction coefficients correlated well with fine particles yet presented higher mass extinction coefficients during the haze episodes (~4.1 $m^2\ g^{-1}$) than other periods (~2.7 $m^2\ g^{-1}$).

Source apportionment of OA by PMF identified three primary OA factors (HOA, COA, and CCOA) and three secondary OA factors (LSOA, SV-OOA, and RSOA). SOA dominated OA for the entire study, on average accounting for 55%. The regional SOA factor (RSOA) was resolved in Beijing for the first time and showed a prominent peak only during Ep3. Although the RSOA accounted for 12% of OA for the entire study, its contribution was up to 26% during Ep3 suggesting that regional transport had played an important role for high OA in this episode. CCOA was the largest primary source, accounting for 19% of OA, followed by HOA (14%) and COA (12%). The OA composition varied dramatically during the four haze episodes and the correlations of OA factors with external tracers, e.g., HOA versus BC, SLOA versus NO_3^-/SO_4^{2-}, were also greatly different between haze and nonhaze episodes indicating the complex sources and processes of aerosol species in this specific January. The regional contributions during the peak of Ep3 were first estimated based on the rapid evolution of aerosol species. It was estimated that regional transport on average contributed 66% of PM_1 during Ep3 and also contributed differently to different aerosol species, among which sulfate and CCOA presented the largest regional contributions, accounting for 75% and 84%, respectively. These results together suggest that stagnant meteorological conditions, coal combustion emissions, secondary production, and regional transport are four dominant factors driving the formation and evolution of winter haze in Beijing.

Acknowledgments

This work was supported by the National Key Project of Basic Research (2014CB447900), the Strategic Priority Research Program (B) of the Chinese Academy of Sciences (grant XDB05020501), and the National Natural Science Foundation of China (41175108). We thank Huabin Dong, Hongyan Chen, Baozhu Ge, and Zhe Wang's help in data comparisons and interpretations, and also the Technical and Service Center, Institute of Atmospheric Physics, Chinese Academy of Sciences, for providing meteorological data. The authors acknowledge the NOAA Air Resources Laboratory (ARL) for the provision of the HYSPLIT transport and dispersion model and/or READY website (http://www.ready.noaa.gov) used in this publication.

References

Aiken, A. C., et al. (2009), Mexico City aerosol analysis during MILAGRO using high resolution aerosol mass spectrometry at the urban supersite (T0)—Part 1: Fine particle composition and organic source apportionment, *Atmos. Chem. Phys.*, *9*(17), 6633–6653.

Allan, J. D., P. I. Williams, W. T. Morgan, C. L. Martin, M. J. Flynn, J. Lee, E. Nemitz, G. J. Phillips, M. W. Gallagher, and H. Coe (2010), Contributions from transport, solid fuel burning and cooking to primary organic aerosols in two UK cities, *Atmos. Chem. Phys.*, *10*(2), 647–668.

An, X., T. Zhu, Z. Wang, C. Li, and Y. Wang (2007), A modeling analysis of a heavy air pollution episode occurred in Beijing, *Atmos. Chem. Phys.*, *7*(12), 3103–3114.

Canagaratna, M. R., et al. (2004), Chase studies of particulate emissions from in-use New York City vehicles, *Aerosol Sci. Technol.*, *38*, 555–573.

Canagaratna, M., et al. (2007), Chemical and microphysical characterization of aerosols via aerosol mass spectrometry, *Mass. Spectrom. Rev.*, *26*, 185–222.

Chen, Y., G. Zhi, Y. Feng, D. Liu, G. Zhang, J. Li, G. Sheng, and J. Fu (2009), Measurements of black and organic carbon emission factors for household coal combustion in China: Implication for emission reduction, *Environ. Sci. Technol.*, *43*(24), 9495–9500.

Clegg, S. L., P. Brimblecombe, and A. S. Wexler (1998), A thermodynamic model of the system H^+-NH_4^+-SO_4^{2-}-NO_3^--H_2O at tropospheric temperatures, *J. Phys. Chem. A*, *102*(12), 2137–2154.

Draxler, R. R., and G. D. Rolph (2013), HYSPLIT (HYbrid Single-Particle Lagrangian Integrated Trajectory) Model access via NOAA ARL READY Website (http://www.arl.noaa.gov/HYSPLIT.php), *NOAA Air Resources Laboratory*, *College Park*, *MD*.

Garland, R. M., et al. (2008), Aerosol optical properties in a rural environment near the mega-city Guangzhou, China: Implications for regional air pollution, radiative forcing and remote sensing, *Atmos. Chem. Phys.*, *8*(17), 5161–5186.

Ge, X., A. Setyan, Y. Sun, and Q. Zhang (2012), Primary and secondary organic aerosols in Fresno, California during wintertime: Results from high resolution aerosol mass spectrometry, *J. Geophys. Res.*, *117*, D19301, doi:10.1029/2012JD018026.

Ge, B., Y. Sun, Y. Liu, H. Dong, D. Ji, Q. Jiang, J. Li, and Z. Wang (2013), Nitrogen dioxide measurement by cavity attenuated phase shift spectroscopy (CAPS) and implications in ozone production efficiency and nitrate formation in Beijing China, *J. Geophys. Res. Atmos.*, *118*, 9499–9509, doi:10.1002/jgrd.50757.

Han, S., et al. (2009), Temporal variations of elemental carbon in Beijing, *J. Geophys. Res.*, *114*, D23202, doi:10.1029/22009JD012027.

Hayes, P. L., et al. (2013), Organic aerosol composition and sources in Pasadena, California during the 2010 CalNex campaign, *J. Geophys. Res. Atmos.*, *118*, 9233–9257, doi:10.1002/jgrd.50530.

Hennigan, C. J., M. H. Bergin, J. E. Dibb, and R. J. Weber (2008), Enhanced secondary organic aerosol formation due to water uptake by fine particles, *Geophys. Res. Lett.*, *35*, L18801, doi:10.1029/12008GL035046.

Herndon, S. C., et al. (2008), Correlation of secondary organic aerosol with odd oxygen in Mexico City, *Geophys. Res. Lett.*, *35*, L15804, doi:10.1029/2008GL034058.

Hu, W. W., et al. (2013), Insights on organic aerosol aging and the influence of coal combustion at a regional receptor site of central eastern China, *Atmos. Chem. Phys.*, *13*(19), 10,095–10,112.

Huang, X. F., et al. (2010), Highly time-resolved chemical characterization of atmospheric submicron particles during 2008 Beijing Olympic Games using an Aerodyne High-Resolution Aerosol Mass Spectrometer, *Atmos. Chem. Phys.*, *10*(18), 8933–8945.

Huang, K., et al. (2012), Typical types and formation mechanisms of haze in an Eastern Asia megacity, Shanghai, *Atmos. Chem. Phys.*, *12*(1), 105–124.

Jayne, J. T., D. C. Leard, X. Zhang, P. Davidovits, K. A. Smith, C. E. Kolb, and D. R. Worsnop (2000), Development of an aerosol mass spectrometer for size and composition analysis of submicron particles, *Aerosol Sci. Technol.*, *33*, 49–70.

Jia, Y., K. A. Rahn, K. He, T. Wen, and Y. Wang (2008), A novel technique for quantifying the regional component of urban aerosol solely from its sawtooth cycles, *J. Geophys. Res.*, *113*, D21309, doi:10.1029/2008JD010389.

Jung, J., H. Lee, Y. J. Kim, X. Liu, Y. Zhang, M. Hu, and N. Sugimoto (2009), Optical properties of atmospheric aerosols obtained by in situ and remote measurements during 2006 Campaign of Air Quality Research in Beijing (CAREBeijing-2006), *J. Geophys. Res.*, *114*, D00G02, doi:10.1029/2008JD010337.

Kaul, D. S., T. Gupta, S. N. Tripathi, V. Tare, and J. L. Collett (2011), Secondary organic aerosol: A comparison between foggy and nonfoggy days, *Environ. Sci. Technol.*, *45*, 7307–7313.

Kebabian, P. L., E. C. Wood, S. C. Herndon, and A. Freedman (2008), A practical alternative to chemiluminescence-based detection of nitrogen dioxide: Cavity attenuated phase shift spectroscopy, *Environ. Sci. Technol.*, *42*(16), 6040–6045.

Kurokawa, J., T. Ohara, T. Morikawa, S. Hanayama, G. Janssens-Maenhout, T. Fukui, K. Kawashima, and H. Akimoto (2013), Emissions of air pollutants and greenhouse gases over Asian regions during 2000–2008: Regional Emission inventory in ASia (REAS) version 2, *Atmos. Chem. Phys.*, *13*(21), 11,019–11,058.

Li, W. J., L. Y. Shao, and P. R. Buseck (2010), Haze types in Beijing and the influence of agricultural biomass burning, *Atmos. Chem. Phys.*, *10*(17), 8119–8130.

Liu, Q. (2012), Physical and chemical characteristics of submicron aerosol and its sources in Beijing, Institute of Atmospheric Physics, Chinese Academy of Sciences.

Liu, X. G., et al. (2013), Formation and evolution mechanism of regional haze: A case study in the megacity Beijing, China, *Atmos. Chem. Phys.*, *13*(9), 4501–4514.

Ma, J., Y. Chen, W. Wang, P. Yan, H. Liu, S. Yang, Z. Hu, and J. Lelieveld (2010), Strong air pollution causes widespread haze-clouds over China, *J. Geophys. Res.*, *115*, D18204, doi:10.1029/2009JD013065.

Matthew, B. M., A. M. Middlebrook, and T. B. Onasch (2008), Collection efficiencies in an Aerodyne Aerosol Mass Spectrometer as a function of particle phase for laboratory generated aerosols, *Aerosol Sci. Technol.*, *42*(11), 884–898.

Ng, N. L., M. R. Canagaratna, J. L. Jimenez, Q. Zhang, I. M. Ulbrich, and D. R. Worsnop (2011a), Real-time methods for estimating organic component mass concentrations from aerosol mass spectrometer data, *Environ. Sci. Technol.*, *45*, 910–916.

Ng, N. L., et al. (2011b), An Aerosol Chemical Speciation Monitor (ACSM) for routine monitoring of the composition and mass concentrations of ambient aerosol, *Aerosol Sci. Technol.*, *45*(7), 770–784.

Paatero, P., and U. Tapper (1994), Positive matrix factorization: A non-negative factor model with optimal utilization of error estimates of data values, *Environmetrics*, *5*, 111–126.

Pan, X. L., et al. (2011), Correlation of black carbon aerosol and carbon monoxide in the high-altitude environment of Mt. Huang in Eastern China, *Atmos. Chem. Phys.*, *11*(18), 9735–9747.

Pereira, S. N., F. Wagner, and A. M. Silva (2011), Seven years of measurements of aerosol scattering properties, near the surface, in the southwestern Iberia Peninsula, *Atmos. Chem. Phys.*, *11*(1), 17–29.

Quan, J., Q. Zhang, H. He, J. Liu, M. Huang, and H. Jin (2011), Analysis of the formation of fog and haze in North China Plain (NCP), *Atmos. Chem. Phys.*, *11*(15), 8205–8214.

Sun, Y., G. Zhuang, A. Tang, Y. Wang, and Z. An (2006), Chemical characteristics of $PM_{2.5}$ and PM_{10} in haze-fog episodes in Beijing, *Environ. Sci. Technol.*, *40*(10), 3148–3155.

Sun, J., Q. Zhang, M. R. Canagaratna, Y. Zhang, N. L. Ng, Y. Sun, J. T. Jayne, X. Zhang, X. Zhang, and D. R. Worsnop (2010), Highly time- and size-resolved characterization of submicron aerosol particles in Beijing using an Aerodyne Aerosol Mass Spectrometer, *Atmos. Environ.*, *44*(1), 131–140.

Sun, Y. L., et al. (2011), Characterization of the sources and processes of organic and inorganic aerosols in New York City with a high-resolution time-of-flight aerosol mass spectrometer, *Atmos. Chem. Phys.*, *11*(4), 1581–1602.

Sun, Y. L., Z. Wang, H. Dong, T. Yang, J. Li, X. Pan, P. Chen, and J. T. Jayne (2012), Characterization of summer organic and inorganic aerosols in Beijing, China with an Aerosol Chemical Speciation Monitor, *Atmos. Environ.*, *51*, 250–259.

Sun, Y. L., Z. Wang, P. Fu, Q. Jiang, T. Yang, J. Li, and X. Ge (2013a), The impact of relative humidity on aerosol composition and evolution processes during wintertime in Beijing, China, *Atmos. Environ.*, *77*, 927–934.

Sun, Y. L., Z. F. Wang, P. Q. Fu, T. Yang, Q. Jiang, H. B. Dong, J. Li, and J. J. Jia (2013b), Aerosol composition, sources and processes during wintertime in Beijing, China, *Atmos. Chem. Phys.*, *13*(9), 4577–4592.

Tao, M., L. Chen, L. Su, and J. Tao (2012), Satellite observation of regional haze pollution over the North China Plain, *J. Geophys. Res.*, *117*, D12203, doi:10.1029/2012JD017915.

Ulbrich, I. M., M. R. Canagaratna, Q. Zhang, D. R. Worsnop, and J. L. Jimenez (2009), Interpretation of organic components from positive matrix factorization of aerosol mass spectrometric data, *Atmos. Chem. Phys.*, *9*(9), 2891–2918.

Wang, C., Y. Yang, Y. Li, and Y. Fan (2013a), Analysis on the meteorological condition and formation mechanism of serious pollution in south Hebei province in January 2013, *Res. Environ. Sci.*, *26*(7), 695–702.

Wang, L. T., Z. Wei, J. Yang, Y. Zhang, F. F. Zhang, J. Su, C. C. Meng, and Q. Zhang (2013b), The 2013 severe haze over the southern Hebei, China: Model evaluation, source apportionment, and policy implications, *Atmos. Chem. Phys. Discuss.*, *13*(11), 28,395–28,451.

Wang, Y., L. Yao, L. Wang, Z. Liu, D. Ji, G. Tang, J. Zhang, Y. Sun, B. Hu, and J. Xin (2014a), Mechanism for the formation of the January 2013 heavy haze pollution episode over central and eastern China, *Sci. China Earth Sci.*, *57*, 14–25.

Wang, Z., et al. (2014b), Modeling study of regional severe hazes over mid-eastern China in January 2013 and its implications on pollution prevention and control, *Sci. China Earth Sci.*, *57*, 3–13.

Watson, J. G. (2002), Visibility: Science and regulation, *J. Air Waste Manage. Assoc.*, *52*(6), 628–713.

Williams, B. J., A. H. Goldstein, N. M. Kreisberg, S. V. Hering, D. R. Worsnop, I. M. Ulbrich, K. S. Docherty, and J. L. Jimenez (2010), Major components of atmospheric organic aerosol in southern California as determined by hourly measurements of source marker compounds, *Atmos. Chem. Phys.*, *10*(23), 11,577–11,603.

Yang, T., Z. Wang, B. Zhang, X. Wang, W. Wang, A. Gbauidi, and Y. Gong (2010), Evaluation of the effect of air pollution control during the Beijing 2008 Olympic Games using Lidar data, *Chin. Sci. Bull.*, *55*(13), 1311–1316.

Zhang, Q., D. R. Worsnop, M. R. Canagaratna, and J. L. Jimenez (2005a), Hydrocarbon-like and oxygenated organic aerosols in Pittsburgh: Insights into sources and processes of organic aerosols, *Atmos. Chem. Phys.*, *5*, 3289–3311.

Zhang, Q., M. R. Alfarra, D. R. Worsnop, J. D. Allan, H. Coe, M. R. Canagaratna, and J. L. Jimenez (2005b), Deconvolution and quantification of hydrocarbon-like and oxygenated organic aerosols based on aerosol mass spectrometry, *Environ. Sci. Technol.*, *39*(13), 4938–4952, doi:10.1021/es048568l.

Zhang, Q., J. L. Jimenez, D. R. Worsnop, and M. Canagaratna (2007), A case study of urban particle acidity and its effect on secondary organic aerosol, *Environ. Sci. Technol.*, *41*, 3213–3219.

Zhang, Q., J. Jimenez, M. Canagaratna, I. Ulbrich, N. Ng, D. Worsnop, and Y. Sun (2011a), Understanding atmospheric organic aerosols via factor analysis of aerosol mass spectrometry: A review, *Anal. Bioanal. Chem.*, *401*, 3045–3067.

Zhang, Y. M., X. Y. Zhang, J. Y. Sun, W. L. Lin, S. L. Gong, X. J. Shen, and S. Yang (2011b), Characterization of new particle and secondary aerosol formation during summertime in Beijing, China, *Tellus B*, *63*(3), 382–394.

Zhang, J. K., Y. Sun, Z. R. Liu, D. S. Ji, B. Hu, Q. Liu, and Y. S. Wang (2013a), Characterization of submicron aerosols during a serious pollution month in Beijing (2013) using an aerodyne high-resolution aerosol mass spectrometer, *Atmos. Chem. Phys. Discuss.*, *13*(7), 19,009–19,049.

Zhang, Z., J. Wang, L. Chen, X. Chen, G. Sun, N. Zhong, H. Kan, and W. Lu (2013b), Impact of haze and air pollution-related hazards on hospital admissions in Guangzhou, China, *Environ. Sci. Pollut. Res.*, *1–9*.

Zhao, X. J., P. S. Zhao, J. Xu, W. Meng, W. W. Pu, F. Dong, D. He, and Q. F. Shi (2013), Analysis of a winter regional haze event and its formation mechanism in the North China Plain, *Atmos. Chem. Phys.*, *13*(11), 5685–5696.